energies

MDPI

Article

Study of Ignition Process in an Aero Engine Combustor Based on Droplet Evaporation Characteristics Analyses

Lei Sun [1], Rui Feng [1], Fangliang Wang [1] and Xiwei Wang [2,*]

[1] Sino-European Institute of Aviation Engineering, Civil Aviation University of China, Tianjin 300300, China; sunlei1988@buaa.edu.cn (L.S.); 2022122008@cauc.edu.cn (R.F.); 2023122049@cauc.edu.cn (F.W.)
[2] Expace Technology Co., Ltd., Wuhan 430040, China
* Correspondence: hcboy_1995@foxmail.com

Abstract: To study the coupling mechanism between droplet evaporation characteristics and flame propagation, in this paper, the ignition process in a single dome lean direct injection combustor is simulated by the Large Eddy Simulation (LES) method. A new concept, i.e., available droplet, and a new parameter, i.e., available equivalence ratio, are innovatively introduced to accurately quantify fuel–air mixing characteristics and reveal flame propagation mechanisms. Simulation results show that the temporal variations in the locally available equivalence ratio during the ignition process can serve as a reliable indicator to identify the flame propagation direction. Moreover, the results show that during the ignition process, available droplets are mainly distributed in the regions where temperatures range from 650 K to 1200 K. The number percentage of available droplets in the combustor increases approximately exponentially to about 2.5% after 40 ms from the ignition. Additionally, the temperature fields and distributions of the available equivalence ratio at different moments during the ignition are also computed and analyzed. The results show that the volume percentage of flammable regions gradually increases from the ignition and eventually stabilizes at about 10% after 8 ms from the ignition. This result shows that during the ignition, the increase in regions whose available equivalence ratios fit flammability is a critical factor for ensuring stable flame development. The available droplet and available equivalence ratio can bridge the gap between droplet-scale evaporation and combustor-scale ignition dynamics, offering an analytical tool for optimizing ignition criteria in aero engine combustors. By analyzing the distributions and evolutions of available fuel rather than fuel vapor, this work can be utilized in design strategies for reliable ignition in extreme conditions.

Keywords: Large Eddy Simulation; ignition process; droplet evaporation; transient flow field

check for updates

Academic Editor: Adonios Karpetis

Received: 27 April 2025
Revised: 3 June 2025
Accepted: 12 June 2025
Published: 14 June 2025

Citation: Sun, L.; Feng, R.; Wang, F.; Wang, X. Study of Ignition Process in an Aero Engine Combustor Based on Droplet Evaporation Characteristics Analyses. *Energies* **2025**, *18*, 3130. https://doi.org/10.3390/en18123130

Copyright: © 2025 by the authors. Licensee MDPI, Basel, Switzerland. This article is an open access article distributed under the terms and conditions of the Creative Commons Attribution (CC BY) license (https://creativecommons.org/licenses/by/4.0/).

1. Introduction

The aero engine is a critical component in modern aircraft due to its significance in both aircraft performance and safety. Among the performance parameters of aero engines, ignition within the combustor has attracted increasing attention in recent years. Studying the ignition processes is essential for aero engines to ensure reliable performance under varying operating conditions. Ignition probability and stability not only affect aero engine startup and stable operation but also play a significant role in emissions control and overall performance [1]. Studies on combustor ignition can be categorized into studies on ignition characteristics, ignition probability, and ignition process. Methodologies to study combustor ignition include experimental approaches, theoretical analyses, and numerical

simulations. Among numerical methods for computational fluid dynamics (CFD) to study practical engineering devices, Reynolds-Averaged Navier–Stokes simulation (RANS) and Large Eddy Simulation (LES) are widely used.

Esclapez et al. [2] utilized LES to calculate ignition probabilities at various locations in a swirl combustor based on cold flow field parameters. The results were validated by premixed, non-premixed, and jet combustion models. Jones et al. [3] utilized LES combined with filtered probability density function (PDF) equations to simulate ignition in an aero engine combustor and further highlighted that the spark size is a critical parameter affecting ignition. Neophytou et al. [4] focused on flame development and estimated ignition probabilities by calculating flame trajectories, which provided a new insight into spark ignition in complex flow fields. Javier et al. [5] proposed local ignition criteria based on the process from kernel formation to successful ignition. They compared the predicted results by local ignition criteria with experimental results and found that the local ignition criteria can be used to obtain acceptable predictions for ignition. Palanti et al. [6] developed a low-order model to provide local ignition probability statistics. Generally speaking, the low-order model may lower the prediction accuracy and affect physical consistency, but the validations by LES simulation data and parameter sensitivity analyses show acceptable performance. In two-phase combustion, droplet characteristics also affect the ignition performances. Liu et al. [7] used the Euler–Lagrange method to simulate high-pressure kerosene injection at environmental pressures ranging from 2.0 to 5.6 MPa using LES. Their results showed that the droplet cluster velocity significantly decreased with increasing environmental pressure. Bulut et al. [8] studied the ignition characteristics of dual-fuel (DF) sprays by LES. In this study, the n-dodecane sprays are injected into methane–air mixtures, and the results showed that DF ignition characteristics are significantly influenced by chemical reaction mechanisms and environmental temperature.

The ignition process is an important branch of studies of ignition characteristics. Tang et al. [9] used a tabulation method to simulate the spark ignition in aviation aero engines under turbulent fuel-stratified conditions. The simulation results for both successful and failed ignition cases were obtained by varying initial spark energy. Thus, the result that ignition characteristics are related to the dynamics of kernel pulses can be obtained. Dong et al. [10] employed a 10 kHz 3D measurement method to study the forced ignition process in liquid-fuel gas turbine model combustors. The key parameters, such as kernel dimensions, structure, growth direction, velocity, and flame propagation speed, were varied to characterize the dynamics of kernel development. Wang et al. [11] utilized RANS to study flame propagation under different ignition positions, identifying the optimal ignition location at the midstream edge of the recirculation zone. Zhao et al. [12] numerically simulated the ignition process in a typical aero engine dual-swirl combustor under various high-altitude flow conditions, fully reproducing the process from fuel atomization to ignition and combustion. Xia et al. [13] used experiments and simulations to study the circumferential ignition process in a multi-nozzle swirl annular combustor, showing that numerical methods can effectively simulate flame propagation in annular combustors. Machover et al. [14] experimentally studied the circumferential ignition and flame propagation of lean propane-air mixtures, comparing the morphological characteristics under two ignition modes: fuel-first, spark-later (FFSL) and spark-first, fuel-later (SFFL).

Some researchers optimized combustor ignition models by improving ignition methods or developing new flame models. Liu et al. [15] used a plasma ignition system to analyze the jet characteristics during plasma discharge based on optical experiments and detailed numerical studies. Moreover, the effects of different plasma parameters on ignition in gas turbine combustors are also explored. Hu et al. [16] implemented a newly proposed similarity mapping spray flamelet/progress variable (SMFPV) model for turbulent spray

combustion, showing that SMFPV is favorable to improving the numerical predictability with acceptable computational cost.

Based on the above review, aero engine combustor ignition is a complicated issue, including the ignition process, ignition characteristics, and ignition probabilities. In the previous studies, fuel-to-air ratio and equivalence ratio distribution in combustors based only on kerosene vapor are calculated and analyzed [17]. However, some kerosene droplets may show properties similar to vapor under certain circumstances [18]. Based on this fact, LES is used to simulate the transient flow field during the ignition process in an aero engine combustor. The parameters "available droplets" and "available equivalence ratio" are introduced to study the effects of the distribution of kerosene vapors and droplets on flame propagation. This analysis method provides a precise tool to study the effects of the local equivalence ratio distribution on the ignition process.

2. Methods and Theories

2.1. Modeling and Meshing

The combustor model utilized in this study is based on the MERCATO test rig [19]. This test rig is utilized for the studies of two-phase combustion in aero engine combustors. As shown in Figure 1, the model is composed of three main sections: a plenum, a combustor, and a depression tube. The swirler is a radial type with 12 blades. The angle between the centerline of the blade and the radial direction is 50°. The fuel nozzle is positioned in the centerline of the combustor and 4 mm from the combustor dome. The combustor is a rectangular structure whose cross-section is a square (129 mm × 129 mm) and length is 500 mm, respectively. Air enters through the plenum and is swirled by the swirler, mixing with kerosene sprays from the nozzle before combustion occurs within the combustor. The coordinate system is shown in Figure 1. The coordinate origin is located at the intersection point of the centerline of the combustor and the plane of the combustor dome. The Z-axis coincides with the centerline of the combustor.

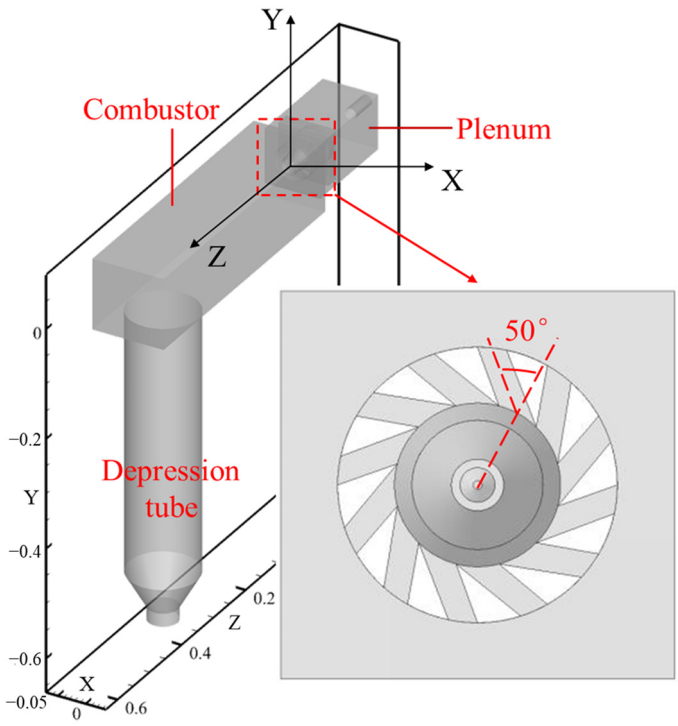


Figure 1. Model of the combustor.

Fluent meshing is used to generate the computational mesh for the combustor model. Specifically, the polyhedral–hexahedral hybrid meshing approach is utilized. Due to the significant variations in flow parameters in the region near the swirler and upstream of the combustor, the mesh is refined in these regions. The mesh size in the refined regions is set as 0.6 mm, while the mesh size in non-refined regions is 1.2 mm. The final mesh distribution is shown in Figure 2.

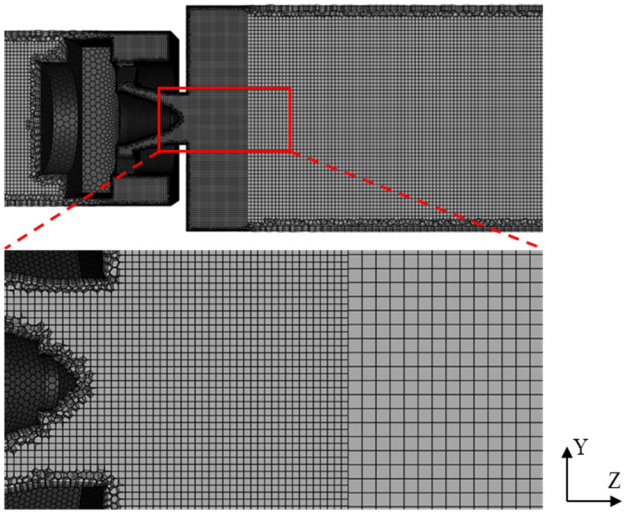


Figure 2. Mesh of the combustor.

2.2. Mesh Independence Analysis

To balance computational accuracy and efficiency, the mesh independence analysis is conducted. Specifically, the mesh in the refined regions is maintained, and the mesh in the left regions is varied to evaluate the effects of the mesh on the flow field parameters. Four types of mesh (total grid numbers are 2.9 million, 6.2 million, 9.3 million, and 12 million, respectively) are analyzed. The mesh independence is verified by comparing the Z-velocity distribution along the Y-direction on the line X = 0 mm at plane Z = 56 mm, as shown in Figure 3. The results indicate that the velocity profiles converge when the grid number exceeds 9.3 million. Therefore, the meshes with the grid number exceeding 9.3 million are chosen for subsequent computations.

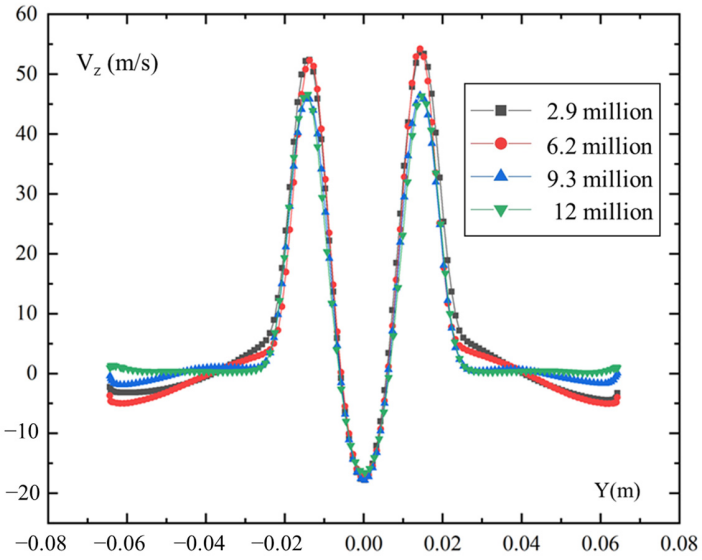


Figure 3. Mesh independence analysis.

2.3. Boundary Conditions and Numerical Methods

The cold flow field simulation of the combustor is first performed using the RANS method. The inlet condition is set as a mass flow inlet with an air mass flow rate of 0.035 kg/s, while the outlet condition is a pressure outlet at 1 atm. Kerosene is used as the fuel, and its atomization process is simulated by the discrete phase model (DPM). The fuel mass flow rate is 0.00225 kg/s, with an injection velocity of 20 m/s, temperature of 300 K, and droplet sizes following a Rosin–Rammler distribution (maximum diameter of 100 μm, minimum diameter of 10 μm, and mean diameter of 50 μm). The atomization type is set as a hollow cone spray with a spray half-angle of 40°. The boundary conditions are summarized in Table 1.

Table 1. Boundary conditions.

Air Mass Flow (kg/s)	Fuel Mass Flow (kg/s)	Temperature (K)	Pressure (Pa)
0.035	0.00225	300	101,325

The LES method is utilized in this paper to simulate the ignition process in the combustor. The filtered control equations are illustrated as follows:

$$\frac{\partial \overline{\rho}}{\partial t} + \frac{\partial \overline{\rho}\widetilde{u_i}}{\partial x_i} = 0 \tag{1}$$

$$\frac{\partial(\overline{\rho}\widetilde{u_i})}{\partial x_i} + \frac{\partial(\overline{\rho}\widetilde{u_i}\widetilde{u_j} + \overline{p}\sigma_{ij})}{\partial x_j} = \frac{\partial(\widetilde{\tau_{ij}} + \tau_{ij}^{SGS})}{\partial x_j} \tag{2}$$

$$\frac{\partial \overline{\rho}\widetilde{h}}{\partial t} + \frac{\partial(\overline{\rho}u_j\widetilde{h})}{\partial x_j} = \frac{D\overline{p}}{Dt} + \frac{\partial}{\partial x_j}\left(\overline{\rho}\alpha\frac{\partial \widetilde{h}}{\partial x_j}\right) + \tau_{ij}\frac{\partial \overline{u_i}}{\partial x_j} \tag{3}$$

$$\frac{\partial \overline{\rho}\widetilde{Y_k}}{\partial t} + \frac{\partial(\overline{\rho}\widetilde{Y_k}u_j)}{\partial x_j} = \frac{\partial}{\partial x_j}\left(\widetilde{\overline{\rho}D_k}\frac{\partial \widetilde{Y_k}}{\partial x_j}\right) + \omega_k \tag{4}$$

In this paper, the WALE model is utilized to model the sub-grid stress. In the WALE model, the sub-grid stress τ_{ij}^{SGS} is calculated as follows:

$$\tau_{ij}^{SGS} = -2\mu_t\left(\widetilde{S}_{ij} - \frac{1}{3}\widetilde{S}_{kk}\delta_{ij}\right) + \frac{2}{3}\overline{\rho}k^{SGS}\delta_{ij} \tag{5}$$

In the WALE model, the eddy coefficient of viscosity μ_t is modeled as follows:

$$\mu_t = \rho L_s^2 \frac{\left(S_{ij}^d S_{ij}^d\right)^{3/2}}{\left(\overline{S}_{ij}\overline{S}_{ij}\right)^{5/2} + \left(S_{ij}^d S_{ij}^d\right)^{5/4}} \tag{6}$$

Calculation methods for DPM can be categorized into the Eulerian method and the Lagrangian method. In the Eulerian method, both air and fuel are treated as continuous phases. In the Lagrangian method, the trajectory of the particles is directly traced. The calculation method for DPM in this paper is the Lagrangian method. The trajectory of the particles in the Lagrangian method is calculated as follows:

$$m_p\frac{d\vec{u}_p}{dt} = m_p\frac{\vec{u} - \vec{u}_p}{\tau_r} + m_p\frac{\vec{g}(\rho_p - \rho)}{\rho_p} \tag{7}$$

where m_p is the droplet mass. τ_r is the relaxation time, which can be determined as follows:

$$\tau_r = \frac{\rho_p d_p^2}{18\mu} \frac{24}{C_d Re} \tag{8}$$

The droplet evaporation model used in this study is the discrete phase droplet evaporation model by Fluent. The droplet convection/diffusion model is expressed as follows:

$$\frac{dm_p}{dt} = k_c A_p \rho_\infty \ln(1 + B_m) \tag{9}$$

where k_c is the mass transfer coefficient. A_p is the droplet surface area. ρ_∞ is the density of bulk gas. B_m is the Spalding mass number given by

$$B_m = \frac{Y_{i,s} - Y_{i,\infty}}{1 - Y_{i,s}} \tag{10}$$

where $Y_{i,s}$ is the vapor mass fraction at the surface of the droplet. $Y_{i,\infty}$ is the vapor mass fraction in the bulk gas.

The droplet temperature is updated according to a heat balance that relates the sensible heat change in the droplet to the convective and latent heat transfer between the droplet and the continuous phase:

$$m_p c_p \frac{dT_p}{dt} = hA_p(T_\infty - T_p) - \frac{dm_p}{dt} h_{fg} + A_p \varepsilon_p \sigma \left(\theta_R^4 - T_p^4\right) \tag{11}$$

where c_p is the droplet heat capacity, T_p is the droplet temperature, h is the convective heat transfer coefficient, T_∞ is the temperature of the continuous phase, dm_p/dt is the rate of evaporation, h_{fg} is the latent heat, ε_p is the particle emissivity, σ is the Stefan–Boltzmann constant, and θ_R is the radiation temperature.

When the droplet temperature reaches the boiling point, a boiling rate equation is applied as follows:

$$\frac{d(d_p)}{dx} = \frac{4k_\infty}{\rho_p c_{p,\infty} d_p} \left(1 + 0.23\sqrt{Re_d}\right) \ln\left[1 + \frac{c_{p,\infty}(T_\infty - T_p)}{h_{fg}}\right] \tag{12}$$

where $c_{p,\infty}$ is the heat capacity of the gas, ρ_p is the droplet density, and k_∞ is the thermal conductivity of the gas.

The reaction mechanism proposed by Franzelli et al. [20] is adopted, which employs a two-step reaction scheme. The corresponding chemical equations are expressed as follows:

$$KERO + 10\,O_2 \rightarrow 10\,CO + 10\,H_2O \tag{13}$$

$$CO + 0.5\,O_2 \rightleftarrows CO_2 \tag{14}$$

In this study, the feasibility of the two-step reaction mechanism for simulating combustor flow fields is verified by comparisons between experimental results and simulated results by detailed chemical kinetic models. Two key parameters, i.e., adiabatic flame temperatures and ignition delay times, are chosen as the evaluation criteria. The detailed validation can be found in our previous study [21].

Subsequent simulations of the cold-flow field and ignition process in the combustor are simulated by LES. The spark is modeled by an Energy Deposit Model (EDM) to replicate realistic spark plug dynamics. The formation of the initial flame kernel is simulated by

introducing a transient energy source term into the energy conservation equation. The equation of this energy source term is expressed as follows:

$$Q(X, Y, Z, t) = \frac{\varepsilon}{4\pi^2\sigma_s^3\sigma_t} e^{-\frac{1}{2}(\frac{r}{\sigma_s})^2} e^{-\frac{1}{2}(\frac{t-t_0}{\sigma_t})^2} \tag{15}$$

where ε is the total energy of the spark, r is the distance from the center of the spark, and t_0 is the time at which the spark attains peak energy deposition. σ_s and σ_t characterize the temporal and spatial scales of energy distribution, respectively, which are determined as follows:

$$\sigma_s = \frac{\Delta s}{4\sqrt{\ln 10}} \tag{16}$$

$$\sigma_t = \frac{\Delta t}{4\sqrt{\ln 10}} \tag{17}$$

where Δs presents the size of the spark, and Δt presents the duration of the spark.

In this study, the ignition process is determined by the following parameters: the duration of the entire ignition event is Δt = 2 ms; the spark center is positioned at the point (0 mm, 57 mm, 56 mm); the maximum diameter of the spherical flame kernel during ignition can reach Δs = 20 mm; the spark is triggered after 40 ms from the initial fuel is injected in the combustor.

In this study, the non-adiabatic steady diffusion flamelet model is utilized to calculate the combustion. Under the assumption of equal diffusivities, the species equations can be reduced to a single equation for the mixture fraction. The Favre mean (density-averaged) mixture fraction equation is as follows:

$$\frac{\partial}{\partial t}\left(\rho\bar{f}\right) + \nabla \cdot \left(\rho\vec{v}\bar{f}\right) = \nabla \cdot \left(\left(\frac{k}{C_p} + \frac{\mu_t}{\sigma_t}\right)\nabla\bar{f}\right) + S_m \tag{18}$$

where k is the laminar thermal conductivity of the mixture, C_p is the mixture specific heat, σ_t is the Prandtl number, and μ_t is the turbulent viscosity. The source term S_m is due solely to the transfer of mass into the gas phase from liquid fuel droplets.

For the LES method, the transport equation is not solved for the mixture fraction variance. Instead, it is modeled as follows:

$$\overline{f'^2} = C_{var} L_s^2 \left|\nabla\bar{f}\right| \tag{19}$$

where C_{var} is fixed at 0.5 in this study, and L_s is the subgrid length scale.

The mixture fraction variance is used in the closure model describing turbulence-chemistry interactions. After diffusion flamelet generation, the flamelet profiles convoluted with the β-PDFs are shown in Equation (20):

$$\overline{\phi} = \iint \phi(f, \chi_{st}) p(f, \chi_{st}) df d\chi_{st} \tag{20}$$

where ϕ represents the mass fractions and temperature of the species. f is the mixture fraction, and χ_{st} is the scalar dissipation at a stoichiometric ratio.

The dimensions of the non-adiabatic PDF tables are as follows: $\overline{T}\left(\bar{f}, \overline{f'^2}, \overline{H}, \overline{\chi_{st}}\right)$, $\overline{Y_i}\left(\bar{f}, \overline{f'^2}, \overline{H}\right)$ for $\chi = 0$, $\overline{Y_i}\left(\bar{f}, \overline{f'^2}, \overline{\chi_{st}}\right)$ for $\chi \neq 0$ and $\overline{\rho}\left(\bar{f}, \overline{f'^2}, \overline{H}, \overline{\chi_{st}}\right)$.

2.4. Validation of LES Mesh Compliance

For LES, the mesh must be validated to meet the computational requirement by using the dimensionless *LRV* number. The computational requirement is that the mesh can

resolve over 80% of the turbulent kinetic energy. *LRV* number is defined as the ratio of the turbulent integral length scale to the mesh cell size. The *LRV* number can be expressed as

$$\mathrm{LRV} = \frac{L_0}{L_c} = \frac{\frac{k^{\frac{3}{2}}}{\varepsilon}}{\sqrt[3]{V_c}} \tag{21}$$

where k is the turbulent kinetic energy, ε is the turbulent dissipation rate, V_c is the mesh cell volume.

The above parameters to calculate the *LRV* number can be determined based on cold flow simulations of the non-reacting flow field in the combustor. The regions where the *LRV* number exceeds 10 indicate that the turbulent integral length scale can include at least 10 grid cells, ensuring a resolution of over 80% of the turbulent kinetic energy [22].

The computational results show that the mesh with a grid number of 12 million can achieve $LRV \geq 10$ throughout the core regions of the combustor except near-wall regions, as illustrated in Figure 4. Near-wall regions exhibit smaller *LRV* values due to strong shear forces that suppress turbulent integral length scales. In order to balance computational cost and accuracy, the Werner–Wengle wall function [23] is utilized to resolve near-wall turbulence. Eventually, the mesh with a grid number of 12 million is adopted for the following study.

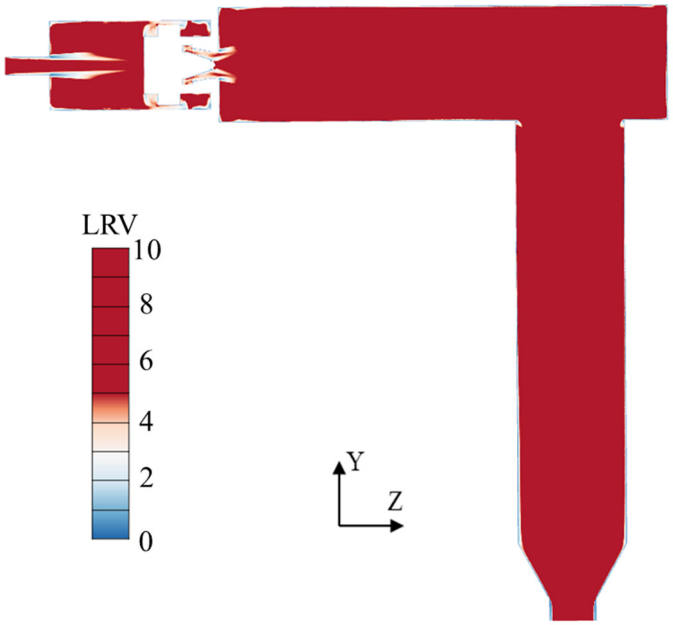


Figure 4. Distribution of *LRV* numbers in the computational mesh with the grid number of 12 million.

2.5. Definition of New Concept and Parameters

In this section, all the subsequent calculations are performed at an individual computational mesh cell level to resolve localized combustion dynamics. By introducing a new concept, "available droplet", and a new parameter, "available equivalence ratio", the analysis method proposed in this paper can accurately quantify fuel–air mixing characteristics and reveal flame propagation mechanisms.

2.5.1. Available Droplet

During the ignition process, the stability and propagation of the flame are controlled by the physical–chemical properties of the fuel in the high-temperature region. The mechanism that maintains stable flame propagation is the heating and evaporation of kerosene droplets in the high-temperature region to form kerosene vapor, which reacts chemically with the

oxidizer. Generally, a high concentration of kerosene vapors in the high-temperature region enhances the stability of flame propagation. However, during the initial stage of the ignition process, a very low concentration of kerosene vapors is due to the insufficient evaporation rate of kerosene droplets in the combustor. Thus, the traditional analyses based on the distribution of kerosene vapors cannot provide an accurate assessment of flame propagation at this stage. In addition, the kerosene vapors generated in the high-temperature region are mainly located inside the flame zone. Therefore, the direction of flame front propagation cannot be determined because the spatial gradient is not well defined.

The concept of "available droplet" is introduced to characterize droplets exhibiting combustion behaviors similar to vapor-phase fuel. Further, the available droplet is defined as a kerosene droplet whose evaporation timescale τ_{eva} is much shorter than its ignition delay time τ_{ign} ($\tau_{eva} \ll \tau_{ign}$).

According to the d^2-law for a single droplet at convective condition, the evaporation time of τ_{eva} is expressed as

$$\tau_{eva} = \frac{{d_0}^2}{K_{conv}} \tag{22}$$

where d_0 and K_{conv} are the initial droplet diameter and convective evaporation coefficient, respectively. Then K_{conv} is determined by

$$K_{conv} = \frac{4\, D_f\, \rho_g}{\rho_l}\, Nu\, \ln(1+B_k) \tag{23}$$

where D_f is the diffusion coefficient of kerosene vapor. ρ_g and ρ_l are the air density and droplet density, respectively. Nu is the Nusselt number, which is determined by Equations (24)–(26). Additionally, B_k is the Spalding number whose expression is shown in Equation (27).

$$Nu = 2 + 0.6 Re^{\frac{1}{2}} Pr^{\frac{1}{3}} \tag{24}$$

where Re and Pr denote the Reynold's number and Prandtl's number, respectively. Re and Pr can be further expressed as

$$Re = \frac{\left|u_g - u_d\right|\, d_0\, \rho_l}{\mu_t} \tag{25}$$

$$Pr = \frac{\mu_t\, Cp_l}{k_g} \tag{26}$$

where u_g and u_d are the gas velocity and droplet velocity, respectively. μ_t is the turbulent viscosity. Cp_l and k_g are the thermal capacity and conductivity of the droplet, respectively.

$$B_k = \frac{Cp_l\, (T_\infty - T_0)}{q_e} \tag{27}$$

where q_e is the latent heat of kerosene. T_∞ and T_0 are the ambient temperature and droplet temperature.

Therefore, the evaporation time τ_{eva} for each droplet can be determined during the ignition process. By comparing the evaporation time τ_{eva} with the local ignition delay time τ_{ign} at the location of each droplet, all available droplets during the ignition process can be determined.

2.5.2. Available Equivalence Ratio

The fuel–air ratio (FAR), which is defined as the ratio of fuel mass flow rate to the air mass flow rate, is an important parameter in aero engine combustor. Generally, the

fuel–air ratio, defined by the total mass flow rate of both fuel and air, has been widely used in previous studies. For scientific analyses, normalized dimensionless parameters are usually favored. Thus, the equivalence ratio is defined as the ratio of the actual FAR to the stoichiometric FAR. Furthermore, the local equivalence ratio is introduced to evaluate the fuel–air distributions within a small region, which is effectively used to analyze flame propagation characteristics. In previous studies of liquid spray combustion, few researchers have considered the contributions of small droplets whose combustion behaviors are similar to vapor phase fuel (i.e., available droplets introduced in Section 2.5.1). Based on physical intuition, the available droplet can be regarded as fuel vapor in many conditions relevant to combustion. In this study, a new parameter, "available equivalence ratio", is proposed to include the effects of available droplets on flame propagation during ignition.

The available equivalence ratio $\phi_{available}$ is defined as

$$\phi_{available} = \frac{FAR_{available}}{FAR_{st}} \tag{28}$$

where $FAR_{available}$ is the available fuel–air ratio. FAR_{st} is the stoichiometric fuel–air ratio.

For the two-step reaction mechanism used in this study, the intermediate species only includes carbon monoxide (CO). Thus, the available fuel consists of three distinct parts: available droplets, kerosene vapor, and CO. Therefore, $FAR_{available}$ is determined as

$$FAR_{available} = \frac{m_{f,available} + m_{f,eva} + m_{CO}}{m_{air}} \tag{29}$$

where $m_{f,available}$, $m_{f,eva}$, m_{CO} are the masses of all available droplets, kerosene vapor, and CO, respectively.

Additionally, the stoichiometric fuel–air ratio FAR_{st} is expressed as

$$FAR_{st} = \frac{m_{f,avaliable} + m_{f,eva} + m_{CO}}{m_{air,st}} \tag{30}$$

where $m_{air,st}$ is the stoichiometric air mass.

For stoichiometric reaction, the correlations between the amount of fuel and oxidizer are shown as

$$C_{10}H_{20} \sim \left(10 + \frac{20}{4}\right)(O_2 + 3.76N_2) \tag{31}$$

$$CO \sim \frac{1}{2}(O_2 + 3.76N_2) \tag{32}$$

Specifically, 1 mol kerosene requires 15 mol of air for a stoichiometric reaction, whereas 1 mol CO requires 0.5 mol of air for a stoichiometric reaction. Therefore, $m_{air,st}$ is determined as

$$m_{air,st} = \left[\left(10 + \frac{20}{4}\right)n_f + \frac{1}{2}n_{CO}\right]\left(M_{O_2} + 3.76M_{N_2}\right) \tag{33}$$

where n_f and n_{CO} are the total amount of available kerosene (available droplets and kerosene vapor) and CO in an individual computational mesh cell. M_{O_2} and M_{N_2} are the molar mass of O_2 and N_2, respectively.

Moreover, n_f and n_{CO} can be expressed as

$$n_f = n_{f,avaliable} + n_{f,eva} = \frac{\sum_i m_{f,avaliable,i} + Y_{f,g}\rho_g V_{cell}}{M_f} \tag{34}$$

$$n_{CO} = \frac{m_{CO}}{M_{CO}} = \frac{Y_{CO}\rho_g V_{cell}}{M_{CO}} \tag{35}$$

where $\sum_i m_{f,avaliable,i}$ is the total mass of the available droplets in an individual computational mesh cell. $Y_{f,g}$ and Y_{CO} are the mass fractions of kerosene vapor and CO, respectively, in an individual computational mesh cell. M_{CO} is the molar mass of CO.

Above all, by calculating the available equivalence ratio for each computational mesh cell, the spatial and temporal distributions of the available equivalence ratio in the combustor can be obtained.

3. Results and Discussions

3.1. Validation of the Reliability of the Numerical Simulation

The reliability of the numerical simulation method is validated by comparing the cold flow field results of the combustor with experimental data from Rosa et al. [24]. Figure 5 shows the cold flow field at the X = 0 mm plane of the combustor. As shown in Figure 5, a recirculation zone forms in the upstream region of the combustor. The black curves represent the contour curves of $v_z = 0 m/s$. It can be observed that the high-speed air ejected from the swirler can form swirling jets and divide the recirculation zone into two parts: the inner recirculation zone (IRZ) and the corner recirculation zone (CRZ). These results agree well with the experimental results from Rosa et al. [24].

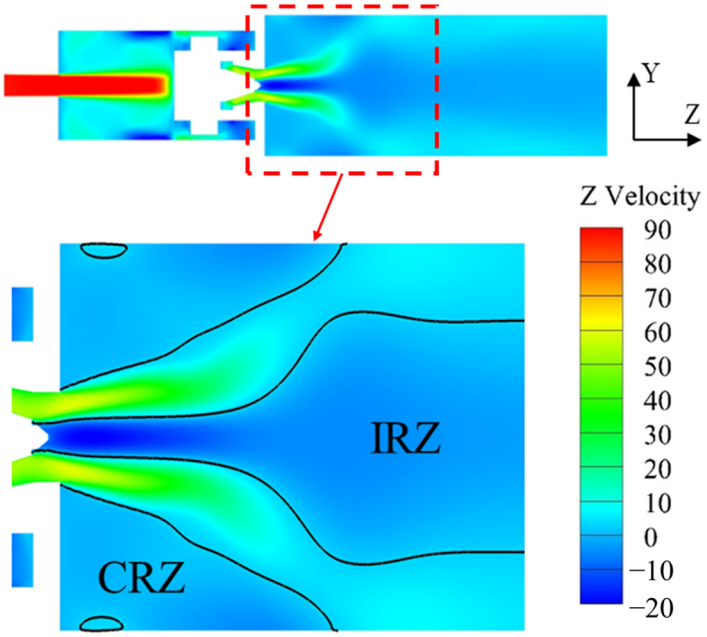


Figure 5. The contour of the cold flow field.

Besides the comparisons of the cold flow field results, the reliability of the numerical simulation method is further verified by comparing the Z-direction velocity along the intersecting line of the plane X = 0 mm and planes Z = 26 mm, Z = 56 mm, and Z = 86 mm, respectively, with experimental data [25], as shown in Figure 6. The comparison results show that in the upstream region of the combustor, the numerical simulation results slightly deviate from the experimental results due to the intense changes in the flow characteristics near the swirler. However, as the flow develops downstream, the numerical simulation results gradually agree well with the experimental data. Therefore, the validation of the reliability of the numerical simulation has been completed.

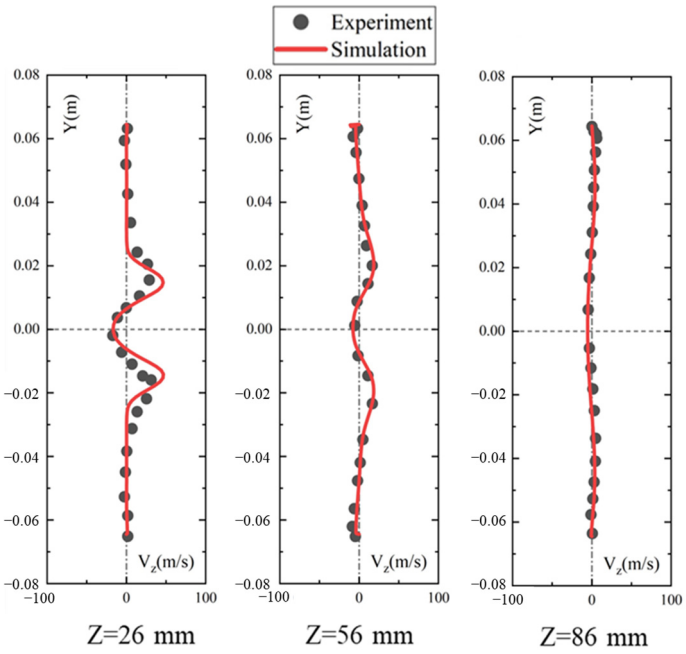


Figure 6. Comparison between experiment and simulation of the cold flow field.

3.2. Pulsation Period

To characterize the flow pulsation frequency in the combustor by LES, temporal variations in axial velocity are monitored at the ignition center (0 mm, 57 mm, 56 mm) before the spark initiation, as shown in Figure 7a. The Fast Fourier Transform (FFT) is utilized to extract frequency information. The result obtained by the FFT is shown in Figure 7b. The spectrogram reveals a dominant pulsation period frequency f = 126.8Hz. The corresponding pulsation period is calculated as $1/f \approx 8$ms, agreeing with the observed experimental combustion pulsation timescale.

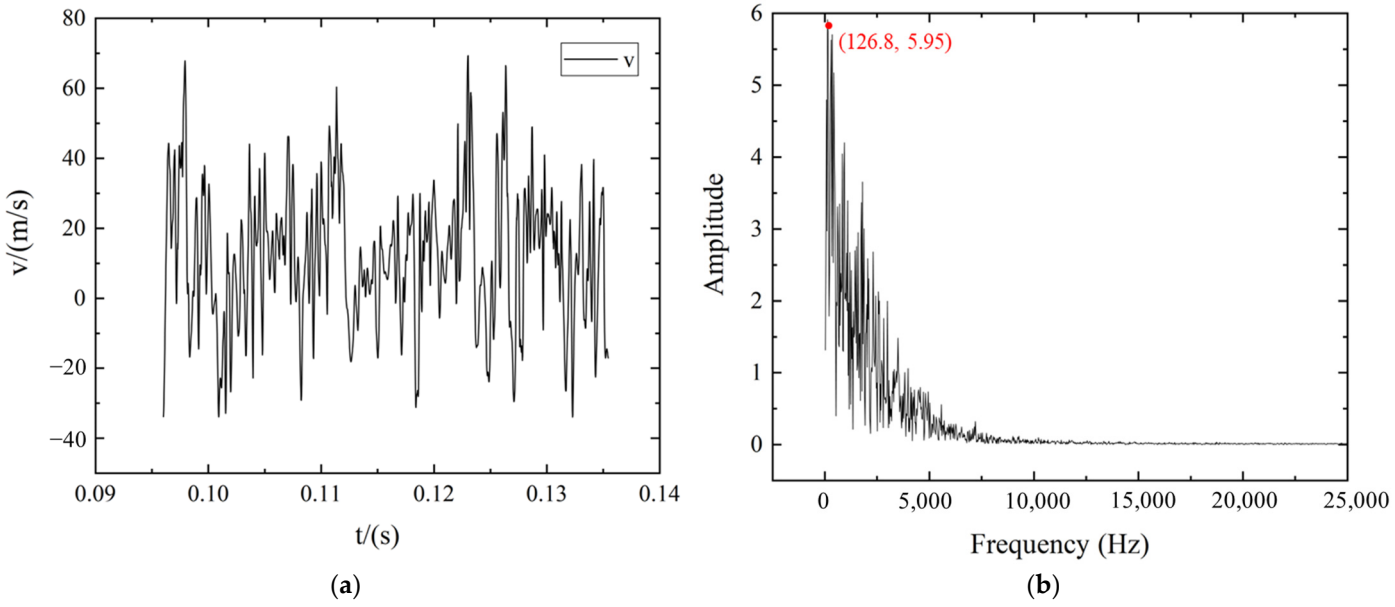


Figure 7. Calculation of pulsation period: (**a**) axial velocity variations at the ignition position; (**b**) Spectrogram of FFT.

3.3. Ignition Process Simulated by LES

The ignition process in the combustor is simulated and analyzed by LES. Figure 8 shows the temperature distribution in the combustor at different moments after ignition. Based on the color scale, some typical corresponding relationships between color and temperature can be determined. The colors of red, yellow, and white represent 1000 K, 1500 K, and 2000 K, respectively. Additionally, in this study, t = 0 ms is defined as the moment when the spark is triggered.

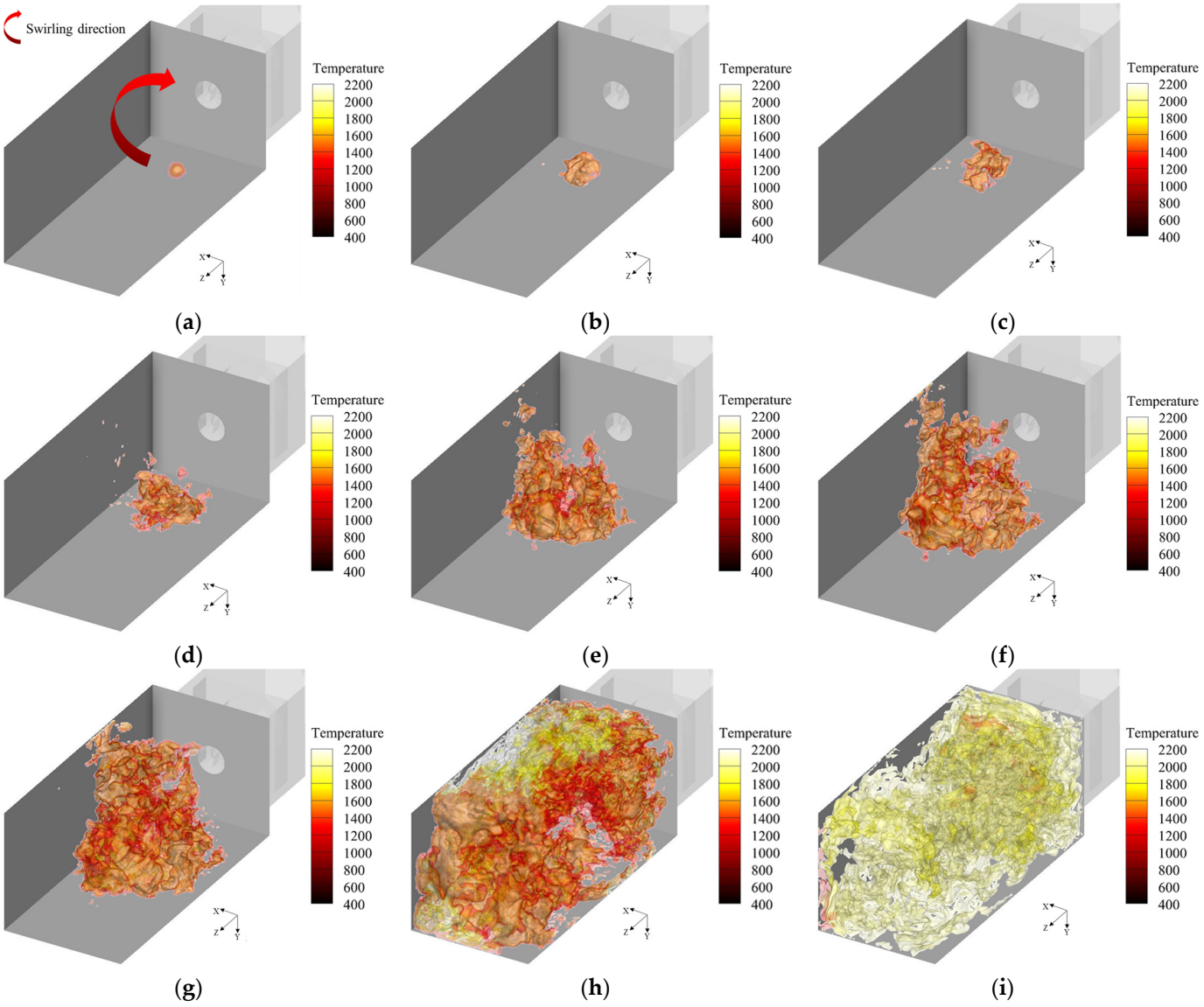


Figure 8. Ignition process simulated by LES: (**a**) t = 1 ms; (**b**) t = 2 ms; (**c**) t = 3 ms; (**d**) t = 5 ms; (**e**) t = 8 ms; (**f**) t = 9 ms; (**g**) t = 10 ms; (**h**) t = 16 ms; (**i**) t = 32 ms.

At t = 1 ms (Figure 8a), a spherical flame kernel is formed near the combustor wall (this position is chosen based on the ignitor location in the real combustors). The highest temperature occurs in the center of the flame kernel, and the temperature decreases with the increase in the radial distance from the center. The red arrow represents both the swirling direction of the airflow in the combustor and the primary propagation direction of the flame.

At t = 2 ms (Figure 8b), the forced ignition phase ends, and the flame kernel begins to expand. The trajectory of flame kernel expansion initially aligns with the swirling airflow in the combustor.

At t = 3 ms (Figure 8c), the flame exhibits expansive and rotational behavior and subsequently propagates both upstream and downstream in the combustor.

At t = 5 ms (Figure 8d), the flame front further propagates and impinges on the combustor side wall.

At t = 8 ms (Figure 8e), the flow time exceeds one pulsation period since the trigger of ignition. The flame front propagating downstream has propagated to the section near Z = 110 mm. Moreover, the axial propagation speed of the flame front propagating downstream increases due to the swirling jet flow development in the downstream region in the combustor. During this period, the flame front propagating circumferentially has rotated 90° in the swirling direction. The flame volume significantly increases compared to the previous moment. Additionally, the flame front propagating upstream spirals to the swirler exit. This phenomenon indicates that during the initial ignition phase, i.e., within one pulsation period, the flow in the combustor is accelerated by the expansion of high-temperature gases. The accelerated hot flow promotes the flame front to propagate quickly towards the downstream region in the combustor.

From t = 9 ms (Figure 8f) to t = 10 ms (Figure 8g), the flame front propagating upstream has reached the swirler exit and ignited the kerosene droplets near the swirler exit, which represents successful ignition.

At t = 16 ms (Figure 8h), the flame front propagating downstream further develops and rotates along the swirling direction. At this moment, the flame is fully filled in the entire combustor. High-temperature regions are mainly distributed near the walls, while the central region of the combustor remains in the low-temperature situation.

At t = 32 ms (Figure 8i), the flame achieves full development. The temperature in major regions is stabilized at around 2000 K except for the dome region. The temperature in the dome region remains relatively lower due to the low-temperature incoming flow of both air and fuel.

Figure 9 shows the comparison of the flame propagation between the experiment by Rosa [24] and the simulation by this study. The iso-surface with a temperature of 1300 K is utilized to describe the flame structure. As the plots show, the simulation results agree well with the experimental data. Thus, the turbulent combustion model used in the simulation is reliable. The validations by comparisons between experimental and simulation results prove the reliability of the computational method and modeling in the present study.

The reaction flow field parameters of stable combustion obtained by numerical simulation and experiment are also compared. Specifically, the Z-direction velocity along the intersecting line of plane X = 0 mm and planes Z = 26 mm, Z = 56 mm, and Z = 86 mm, respectively, are compared with experimental data [25], as shown in Figure 10. The comparison indicates that in the upstream region of the combustor, the numerical simulation results slightly deviate from the experimental results due to the intense changes in the flow characteristics near the swirler. As the flow develops, the simulation results gradually agree well with the experimental data in the downstream region in the combustor. These results further verify the reliability that LES can be utilized to simulate and analyze the ignition process.

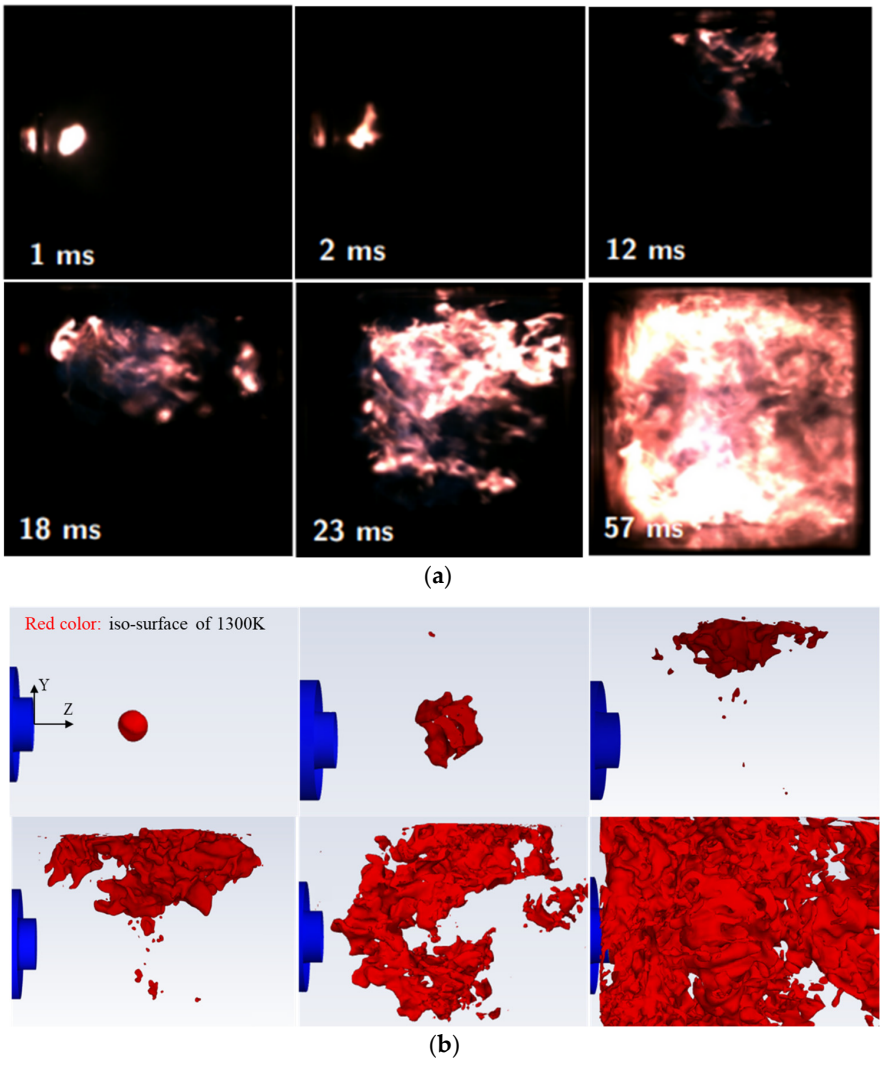


Figure 9. Validation in flame structure: (**a**) experiment results; (**b**) simulation results.

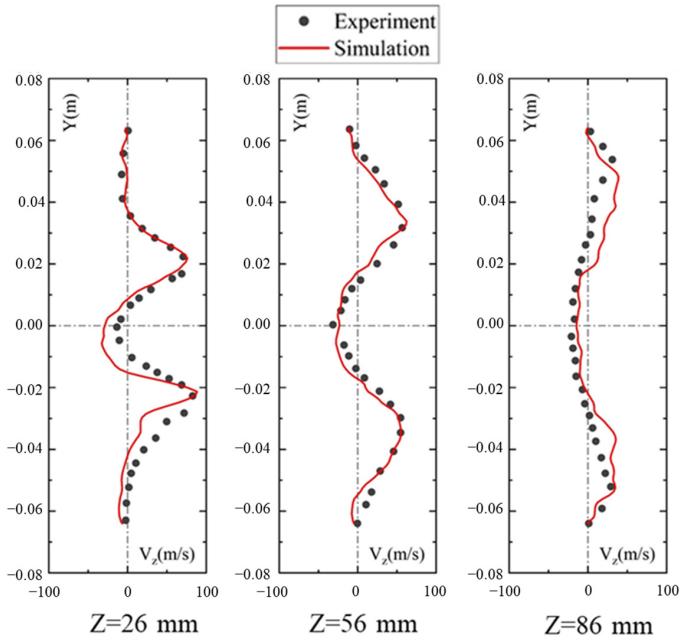


Figure 10. Comparison between the hot flow time-averaged field obtained by LES and experimental results.

3.4. Ignition Process Analyses Based on Available Equivalence Ratio

The available equivalence ratio can significantly affect the local combustion stability in the combustor. Then, the local combustion stability directly determines the result of ignition, success or failure. In this study, the ignition performance is analyzed based on the available equivalence ratio at various moments after the trigger of the spark.

Figure 11 shows the distribution of the available equivalence ratio and temperature field in the combustor at different moments after the trigger of the spark. Similar to Figure 8, the warm color scale represents temperature, and the cold color scale represents the available equivalence ratio. The discrete blue regions represent kerosene droplet clusters and kerosene vapors around them, whereas the continuous blue regions mainly represent the gaseous fuel (kerosene vapor and CO).

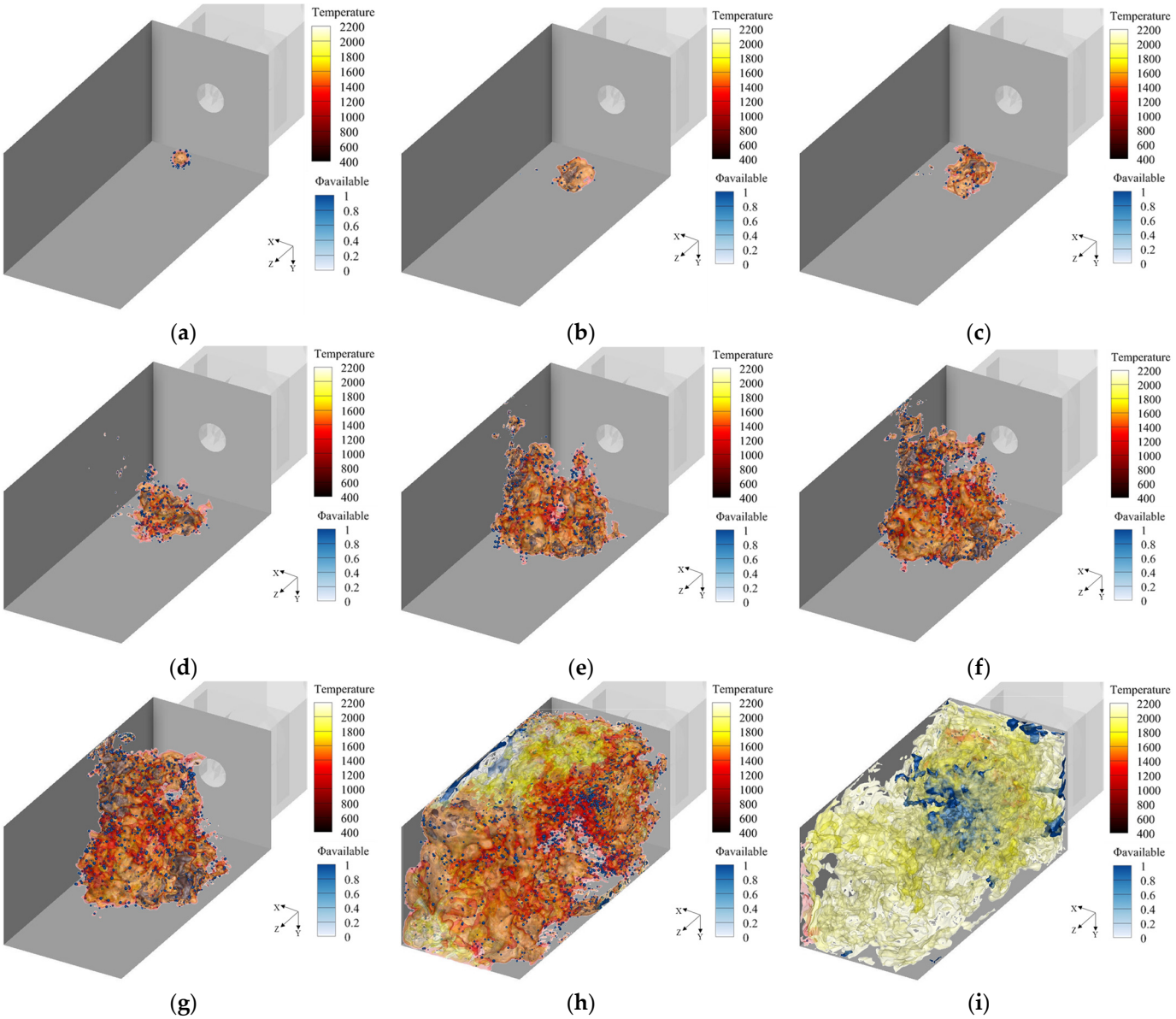


Figure 11. Variation in the distribution of available equivalence ratio during the ignition process: (**a**) t = 1 ms; (**b**) t = 2 ms; (**c**) t = 3 ms; (**d**) t = 5 ms; (**e**) t = 8 ms; (**f**) t = 9 ms; (**g**) t = 10 ms; (**h**) t = 16 ms; (**i**) t = 32 ms.

At t = 1 ms (Figure 11a), a spherical flame kernel is formed. At this early stage, no kerosene vapor or intermediate product CO is generated in the flame kernel. However,

discrete blue regions near the 1000 K iso-surface occur, which indicates the existence of available droplets. The available droplets can rapidly evaporate within the ignition delay time, ensuring the flame kernel expands outwards and ignites the surrounding region.

At t = 2 ms (Figure 11b), the forced ignition phase ends. The high-temperature region begins to generate available gaseous fuel, including kerosene vapor and carbon monoxide. There is sufficient combustible gas in the regions enclosed by the 2000 K iso-surface, indicating that stable reactions in this region can release sufficient heat and then significantly enhance the environmental temperature and further generate more available droplets.

From t = 3 ms (Figure 11c) to t = 5 ms (Figure 11d), the flame propagates further along the recirculation zone to the dome of the combustor. The flame propagates to the regions near the flame where the high available equivalence ratio exists before the flame front arrives. The development of high-temperature regions leads to an increase in the high available equivalence ratio regions. In Figure 11d, the range of high temperature decreases on the plane X = 0 mm as the flame propagates circumferentially. However, sufficient available droplets still exist on this plane to ensure stable combustion. At these moments, the high-temperature region is mainly distributed near the walls, and sufficient combustible gas exists in the region enclosed by the 2000 K iso-surface. There are sufficient clusters of available droplets to support flame propagation along the walls.

At t = 8 ms (Figure 11e), the flame fully propagates along CRZ to the side wall and upstream regions in the combustor. The high-temperature region is mainly located near the side wall in the CRZ. Thus, heat accumulates in the CRZ and enhances the temperature in the CRZ. This process can generate sufficient available droplets to support the flame to propagate to the dome of the combustor through the CRZ.

At t = 9 ms (Figure 11f), the flame will soon arrive at the swirler exit. At this moment, there are high available equivalence ratio regions between the swirler exit and the flame front, which ensures that the flame propagates to the swirler exit.

At t = 10 ms (Figure 11g), the flame front arrives at the swirler exit, leading to intense and full mixing of the high-temperature burned gas and the unburned incoming mixture near the flame stabilization zone. Once the flame stabilizes at the stabilization zone, sufficient available droplets can form continuously, thus increasing the available equivalence ratio in the IRZ.

At t = 16 ms (Figure 11h), the flame front propagating circumferentially rotates nearly a full circle, and the flame almost fills the entire combustor. However, the flame does not achieve full development at this stage, with the low-temperature CRZ containing a large number of available droplets. At this moment, high temperature as well as high concentration combustible gas regions are mainly located at the downstream region, dome region, and near wall region.

At t = 32 ms (Figure 11i), the flame achieves full development. Available fuels whose main component is combustible gas are mainly located in the CRZ. However, few available fuels exist in the downstream high-temperature regions. For stable combustion, the droplets rapidly evaporate and form a combustible mixture once they are injected into the combustor. The combustible mixture burns and generates high-temperature gases as they flow downstream with the main flow stream. On the other hand, a part of high-temperature gases is entrained into the recirculation zone by turbulence and flow upstream to serve as a heat source to promote the evaporation and combustion of the subsequent unburned incoming mixture. This self-sustaining process is the key to flame propagation and stable combustion.

In summary, compared to the traditional equivalence ratio, the variation in the available equivalence ratio during the ignition process provides a more insightful understanding

of the effects of fuel distribution on flame propagation. The spatial and temporal distribution of the available equivalence ratio, coupled with the flow field and temperature field, can give reasonable explanations for flame development during the ignition process. The above analysis methods provide an important tool for optimizing ignition strategies, improving combustion efficiency, and ensuring stable combustion in practical combustion systems.

3.5. Analyses of Available Droplet Characteristics

In order to study the characteristics of the new concept, i.e., available droplets during the ignition process, the diameter distribution of available droplets at each moment after ignition is obtained, as shown in Figure 12. In these bar charts, each bar represents the percentage of available droplets within a specific diameter range relative to the total number of available droplets in the combustor at each moment after ignition. As shown in these subfigures, the diameters of the majority of available droplets during the ignition process are below 70 μm. At t = 1 ms (Figure 12a), the diameters of the highest percentage of available droplets in the combustor range from 20 μm to 30 μm, with a percentage of about 26.8%. As the flame develops, the increased flame volume allows larger droplets to evaporate rapidly within the ignition delay time, making larger diameter droplets available. At t = 3 ms (Figure 12b), the diameters of the highest percentage of available droplets in the combustor range from 30 μm to 40 μm, with a percentage of about 18.5%. At t = 5 ms (Figure 12c), the diameters of the highest percentage of available droplets in the combustor range from 40 μm to 50 μm, with a percentage of about 16%. After t = 8 ms (Figure 12d), the diameter distributions of available droplets remain almost unchanged.

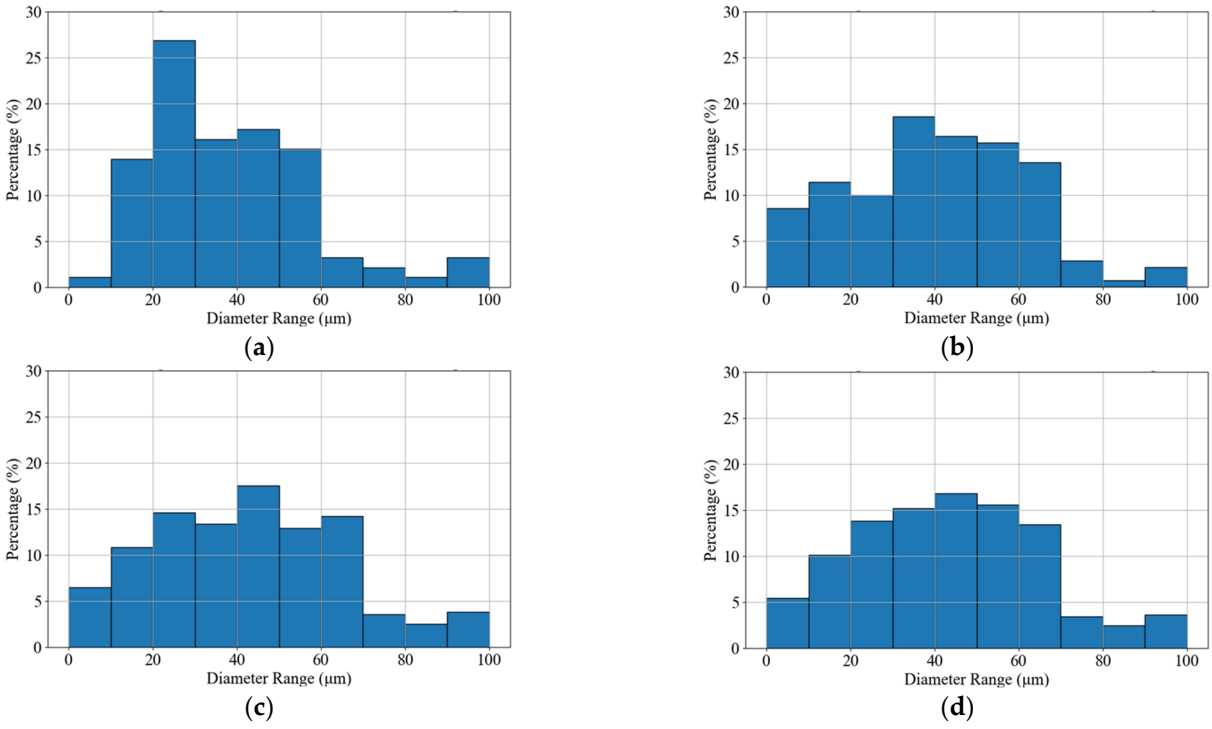


Figure 12. Diameter distributions of available droplets at moments after ignition: (**a**) t = 1 ms; (**b**) t = 3 ms; (**c**) t = 5 ms; (**d**) t = 8 ms.

Figure 13 shows the relationship between the diameters of available droplets and temperature distributions in the combustor at t = 5 ms. Most of the available droplets (about 89.2%) concentrate in the regions where temperatures range from 650 K to 1200 K. Moreover, larger diameter available droplets (i.e., the diameter is larger than 40 μm) exist in regions with the same temperature ranges, i.e., range from 650 K to 1200 K. In

the regions where T > 1200 K, available droplets account for only about 3% of the total droplets, which is attributed to the ignition delay time decreasing exponentially with the increasing temperature. When the ignition delay time is very short, only small droplets can evaporate completely and participate in combustion, whereas large droplets cannot evaporate completely and are classified as unavailable. In the regions where T < 650 K, the droplets evaporate slowly and cannot generate enough combustible mixture in a relatively big region in the combustor. The flame can only occur near the droplets and be sensitive to the low-temperature flow around it. In the regions where the temperatures range from 650 K to 1200 K, small and medium droplets (d_0 < 40 μm) dominate the fuel vapor supply, as they evaporate fully before ignition. Thus, optimizing atomization can ensure more droplets reach the "available" range and further enhance the ignition reliability. In high-temperature regions, ignition occurs almost instantaneously, leaving insufficient time for large droplets to evaporate. Unevaporated large droplets act as heat sinks, locally reducing temperatures and disrupting flame propagation. Large droplets entrained into high-temperature regions are either convected away or broken up into smaller droplets due to aerodynamic shear.

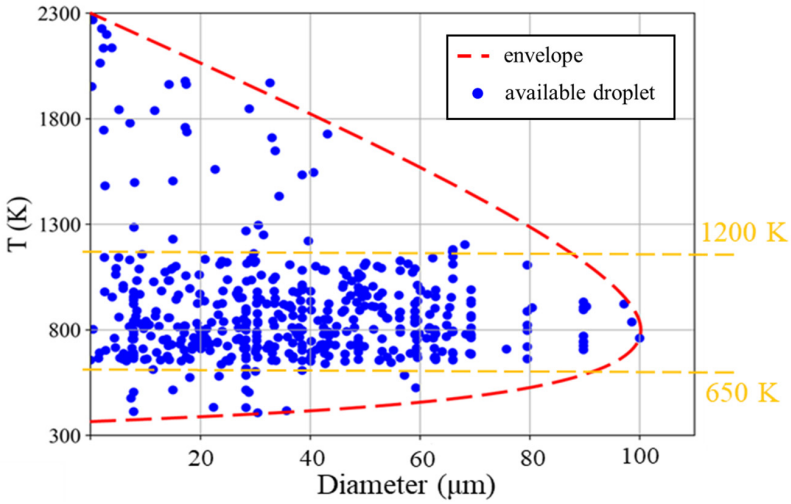


Figure 13. Relationship between diameters of available droplets and temperature distribution at t = 5 ms.

Figure 14 quantifies the dynamic evolution of the number percentage of available droplets with time after ignition in the combustor. It reveals that the number percentage of available droplets $\eta_{available}$ increases nonlinearly (approximately exponentially) as the flame develops. As shown in Figure 14, at the end of the first pulsation cycle, i.e., 8 ms, $\eta_{available}$ is still below 0.5%. Then, the increased speed of $\eta_{available}$ increases with the flame development. Eventually, $\eta_{available}$ stabilizes at about 2.5% with small fluctuations at t = 24 ms, which can be attributable to the achievement of thermal equilibrium in the combustor when the combustion sustains stably after ignition. From t = 0 ms to t = 8 ms, temperatures rise from approximately 800 K to 1200 K in the preheating zones. τ_{ign} decreases slowly, leading to a slow increase in $\eta_{available}$. From t = 8 ms to t = 24 ms, temperatures in the preheating zones rise to approximately 1500 K. Under this condition, τ_{ign} decreases exponentially, while τ_{eva} decreases linearly, leading to a rapid increase in $\eta_{available}$. After t = 24 ms, temperatures reach the nearly stable values. Under this condition, the smaller droplets fully evaporate, while larger droplets transport into the "available" size range due to continuous evaporation. Thus, $\eta_{available}$ reach a nearly stable value due to evaporation–combustion equilibrium. This result verifies that the approximate exponential number percentage of available droplets is a requisite for a successful ignition.

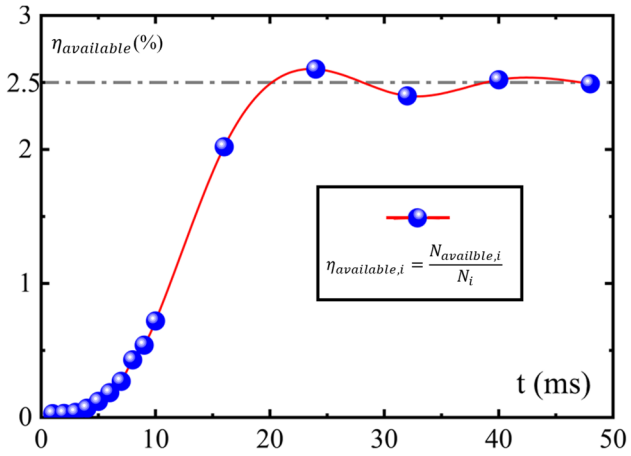


Figure 14. Variation in number percentage of available droplets with time after ignition.

3.6. Analyses of Available Equivalence Ratio Characteristics

Based on LES coupled with a simplified two-step reaction mechanism, when the global equivalence ratio is set as 0.95, the computational adiabatic flame temperature in the combustor is approximately 2300 K, which is approximately equal to the theoretical value of adiabatic flame temperature. Based on the correlation between the temperature gradient and the chemical reaction process, the internal regions in the flame can be further divided into the burned region and the preheating region, as shown in Figure 15. The burned region, where temperatures are about 2300 K, can achieve complete combustion and sustain a thermal equilibrium state. Thermal equilibrium analyses can reveal that the burned region is filled with a lot of fully oxidized products and a small amount of unreacted intermediates, which means that kerosene vapors are entirely consumed in this region. The preheating region, where temperatures range from 650 K to 2300 K, serves as the precursor for intense reactions and is characterized by significant coupling of heat, mass transfer, and phase changes. When the temperatures range from 650 K to 1300 K, the generation of kerosene vapor from available droplets is dominated by evaporation, coupling closely to turbulence in the flow field. When the temperatures range from 1300 K to 2300 K, kerosene vapor undergoes the following processes, i.e., premixing, oxidation, producing intermediate product CO, and releasing heat.

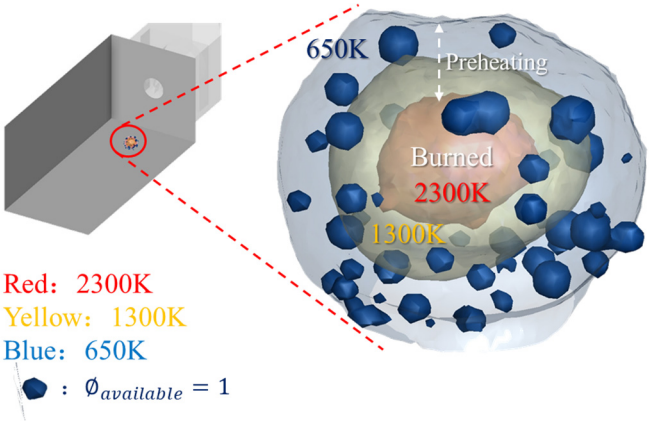


Figure 15. Schematic of burned zone and preheating zone.

The flammable limit of a fuel is a critical parameter to determine whether the stable combustion can be maintained under specific conditions. Generally, the flammable limit consists of the upper and lower fuel vapor concentration thresholds at which combustion can be sustained by the analyses of both conservation of energy and chemical reaction

kinetics [26]. For a hydrocarbon fuel with the chemical formula C_nH_m, the volume fraction of oxygen required for complete combustion, denoted as C_{st}, can be expressed as follows:

$$C_{st} = \frac{100}{1 + 4.773\left(n + \frac{m}{4}\right)} \tag{36}$$

The upper flammable limit at 25 °C U_{25} and lower flammable limit at 25 °C L_{25} are expressed as follows:

$$U_{25} = \frac{1}{0.01337n + 0.05151} \tag{37}$$

$$L_{25} = \frac{1}{0.1347n + 0.04343} \tag{38}$$

In this study, the chemical formula of the kerosene is $C_{10}H_{20}$. Based on Equations (36)–(38), the flammable limits [L, U] can be quantitatively expressed as follows:

$$U = \frac{U_{25}}{C_{st}} = \frac{5.399}{1.3775} = 3.92 \tag{39}$$

$$L = \frac{L_{25}}{C_{st}} = \frac{0.7192}{1.3775} = 0.52 \tag{40}$$

Thus, based on the analyses of flammability in the combustor, the variation in volume percentage of flammable regions $\eta_{flammable}$ with time after ignition can be shown in Figure 16. In the early ignition stage, after the trigger of the spark, $\eta_{flammable}$ grows slowly and reaches 1.72% at t = 3 ms, indicating that most regions in the combustor are in fuel-lean conditions. At this moment, the flame kernel starts to expand and does not fully develop; the spatial-temporal non-uniformities of droplet evaporation and fuel–air mixing lead to the discrete local equivalence ratio distributions. After t = 3 ms, the flame reaches a self-sustained propagation phase, and the flammable region grows rapidly to 10.21%. During this stage, the increased heat release elevates the flow field temperature and improves the droplet evaporation. Moreover, turbulence enhances fuel–air mixing, enabling more regions to reach the flammable condition. After t = 8 ms, $\eta_{flammable}$ stabilizes at about 10% with small fluctuations. Then, high-temperature regions and droplet evaporation achieve a dynamic balance state and further sustain the stable combustion. This study shows that the rapid growth and subsequent stabilization of the flammable region are key indicators of the transition from initial ignition to stable flame propagation.

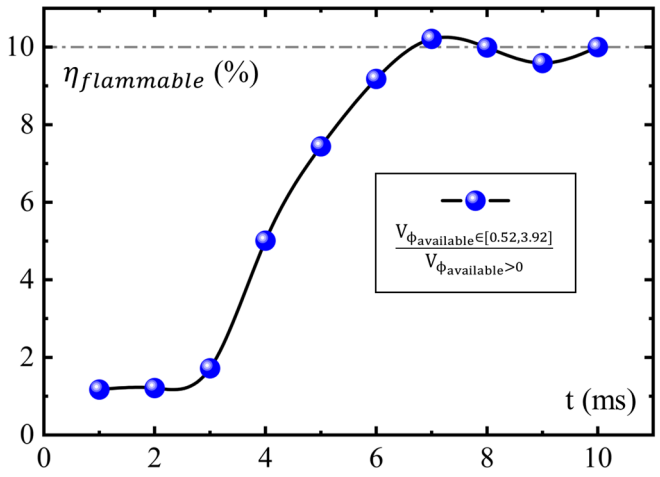


Figure 16. Variation in volume percentage of flammable regions with time after ignition.

4. Conclusions

In this paper, the LES method is utilized to study the transient flow field characteristics during the ignition process in an aero engine combustor based on the MERCATO test rig. Firstly, the simulation results of the cold flow field and the stable combustion flow field are compared with experimental results to validate the analysis methods. Furthermore, a new concept, i.e., available droplet, and a new parameter, i.e., available equivalence ratio, are introduced innovatively to analyze the effects of the droplet characteristics on flame propagation during the ignition process. Some conclusions can be obtained as follows:

(1) Flame propagation during ignition is closely related to the regions with high available equivalence ratios. In the early ignition stage, available droplets rapidly increase around the flame kernel, ensuring the development of the flame kernel. As ignition progresses, sufficient combustible gases, including kerosene vapor and CO, are gradually generated in the flame region to maintain the flame expansion and finally fill in the whole combustor to achieve stable combustion.

(2) Most of the available droplets (about 89.2%) concentrate in the regions where the temperatures range from 650 K to 1200 K. Moreover, larger diameter available droplets (i.e., the diameter is larger than 40 μm) also only exist in the regions with this same temperature range. Apart from this temperature range, just a few of the available droplets exist.

(3) The number percentage of available droplets increases approximately exponentially as the flame develops and eventually stabilizes at about 2.5%.

(4) The volume percentage of flammable regions increases slowly at the early ignition stage and then increases rapidly at the flame self-sustain propagation stage and eventually stabilizes at about 10%.

(5) The new concepts proposed in this paper (available droplet and available equivalence ratio) bridge the gap between droplet-scale evaporation and combustor-scale ignition dynamics, offering an analytical tool for optimizing ignition criteria in aero engine combustors. By analyzing the distributions and evolutions of available fuel rather than fuel vapor, this work can be utilized in design strategies for reliable ignition in extreme conditions.

Author Contributions: L.S.: writing—reviewing, supervision, validation. R.F.: administration, methodology, software, simulation, data curation, investigation, writing—original draft preparation. F.W.: writing—reviewing, validation. X.W.: writing—reviewing, supervision, validation. All authors have read and agreed to the published version of the manuscript.

Funding: This work is supported by the National Natural Science Foundation of China (Grant No. 52306176), Support Fund to the National Natural Science Foundation of China from Civil Aviation University of China (No. 3122024PT28), Tianjin Science and Technology Plan Project (Grant No. 23JCQNJC00260), Tianjin Education Commission Research Program Project (Grant No. 2022KJ071).

Data Availability Statement: The data presented in this study are available on request from the corresponding author.

Conflicts of Interest: Author Xiwei Wang was employed by the company Expace Technology Co., Ltd. The remaining authors declare that the research was conducted in the absence of any commercial or financial relationships that could be construed as a potential conflict of interest.

Abbreviations

The following abbreviations are used in this manuscript:

LES	Large eddy simulation
RANS	Reynolds-Averaged Navier–Stokes simulation
DPM	Discrete phase model
EDM	Energy deposit model
CRZ	Corner recirculation zone
IRZ	Inner recirculation zone
FFT	Fast Fourier transport

References

1. Swithenbank, J. Combustion design fundamentals. In *Symposium on Combustion*; Elsevier: Amsterdam, The Netherlands, 1973; Volume 14.
2. Esclapez, L.; Collin, B.F.; Riber, E. A statistical model to predict ignition probability. *Combust. Flame* **2021**, *225*, 180–195. [CrossRef]
3. Jones, W.P.; Tyliszczak, A. Large eddy simulation of spark ignition in a gas turbine combustor. *Flow Turbul. Combust.* **2010**, *85*, 711–734. [CrossRef]
4. Neophytou, A.; Richardson, E.S.; Mastorakos, E. Spark ignition of turbulent recirculating non-premixed gas and spray flames: A model for predicting ignition probability. *Combust. Flame* **2012**, *159*, 1503–1522. [CrossRef]
5. Javier, M.S.; Felix, C.B.; Riber, E. On the mechanisms of flame kernel extinction or survival during aeronautical ignition sequences: Experimental and numerical analysis. *Combust. Flame* **2020**, *222*, 70–84.
6. Palanti, L.; Andreini, A.; Facchini, B. Numerical prediction of the ignition probability of a lean spray burner. *Int. J. Spray Combust. Dyn.* **2021**, *13*, 96–109. [CrossRef]
7. Liu, T.; Xiong, Y.; Zhao, D. Large eddy simulations of high-pressure rocket propellant# 3 aviation kerosene spay in pressurized quiescent environments. *Energy Sources Part A Recovery Util. Environ. Eff.* **2025**, *47*, 10380–10395.
8. Tekgul, B.; Kahila, H.; Kaario, O.; Vuorinen, V. Large-eddy simulation of dual-fuel spray ignition at different ambient temperatures. *Combust. Flame* **2020**, *215*, 51–65. [CrossRef]
9. Tang, Y.; Hassanaly, M.; Raman, V.; Sforzo, B.A.; Wei, S.; Seitzman, J.M. Simulation of gas turbine ignition using large eddy simulation approach. In *Turbo Expo: Power for Land, Sea, and Air*; American Society of Mechanical Aeroengineers: New York, NY, USA, 2018; Volume 51067, p. V04BT04A007.
10. Dong, R.; Lei, Q.; Zhang, Q.; Fan, W. Dynamics of ignition kernel in a liquid-fueled gas turbine model combustor studied via time-resolved 3D measurements. *Combust. Flame* **2021**, *232*, 111566. [CrossRef]
11. Wang, K.; Fan, X.; Liu, F. Experimental Studies on Fuel Spray Characteristics of Pressure-Swirl Atomizer and Air-Blast Atomizer. *J. Therm. Sci.* **2021**, *30*, 729–741. [CrossRef]
12. Zhao, Q.; Yang, J.; Mu, Y.; Li, Y.; Liu, C.; Liu, F.; Xu, G. Experimental investigation of flow field features and spark ignition process in a multi-swirl air blast injector. *Fuel* **2021**, *306*, 121732. [CrossRef]
13. Xia, Y.; Zheng, Y.; Zhao, D.; Ge, H.; Wang, G. Numerical Simulations of the ignition dynamics in an annular combustor. In Proceedings of the 13th World Congress on Computational Mechanics, New York, NY, USA, 22–27 July 2018.
14. Machover, E.; Mastorakos, E. Experimental investigation on spark ignition of annular premixed combustors. *Combust. Flame* **2017**, *178*, 148–157. [CrossRef]
15. Liu, S.; Zhao, N.; Zhang, J.; Yang, J.; Li, Z.; Zheng, H. Experimental and numerical investigations of plasma ignition characteristics in gas turbine combustors. *Energies* **2019**, *12*, 1511. [CrossRef]
16. Hu, Q.; Wang, L. Turbulent spray combustion modeling in reduced tabulation parameter space by similarity map. *Combust. Flame* **2024**, *270*, 113749. [CrossRef]
17. Yu, D.; Chen, Z. Premixed flame ignition: Theoretical development. *Prog. Energy Combust. Sci.* **2024**, *104*, 101174. [CrossRef]
18. Huang, Y.; Lin, Y.; Fan, W. *Combustion and Combustion Chamber*; Beijing University of Aeronautics and Astronautics Press: Beijing, China, 2009; pp. 296–300.
19. Rosa, N.G. *Ignition Phenomena of a Turbomachine Combustor Under High-Altitude Conditions*; ISAE: Toulouse, France, 2008.
20. Franzelli, B.; Riber, E.; Sanjosé, M.; Poinsot, T. A two-step chemical scheme for kerosene–air premixed flames. *Combust. Flame* **2010**, *157*, 1364–1373. [CrossRef]
21. Sun, L.; Zhang, H.; Wang, F.; Feng, R. Flow field near lean blowout in a single point lean direct injection combustor based on large eddy simulation. *J. Propuls. Technol.* **2025**, *46*, 2404017. (In Chinese)
22. Zhang, B.; Wang, T.; Gu, C.; Dai, Z. A novel meshing approach for large eddy simulation. In Proceedings of the Fluids Engineering Division Summer Meeting, Montreal, QC, Canada, 1–5 August 2010; pp. 2527–2535.

23. Werner, H.; Wengle, H. Large-eddy simulation of turbulent flow over and around a cube in a plate channel. In *Turbulent Shear Flows 8: Selected Papers from the Eighth International Symposium on Turbulent Shear Flows, Munich, Germany, 9–11 September 1991*; Springer: Berlin/Heidelberg, Germany, 1991; pp. 155–168.
24. Rosa, N.G.; Linassier, G.; Lecourt, R.; Villedieu, P.; Lavergne, G. Experimental and numerical study of high-altitude ignition of a turbojet combustor. *Heat Transf. Aeroengineering* **2011**, *32*, 949–956. [CrossRef]
25. Hervo, L.; Senoner, J.M.; Biancherin, A. Large-Eddy Simulation of Kerosene Spray Ignition in a Simplified Aeronautic Combustor. *Flow Turbul. Combust.* **2018**, *101*, 603–625. [CrossRef]
26. Zabetakis, M.G. *Flammability Characteristics of Combustible Gases and Vapors*; Bureau of Mines: Pittsburgh, PA, USA, 1964.

Disclaimer/Publisher's Note: The statements, opinions and data contained in all publications are solely those of the individual author(s) and contributor(s) and not of MDPI and/or the editor(s). MDPI and/or the editor(s) disclaim responsibility for any injury to people or property resulting from any ideas, methods, instructions or products referred to in the content.